

# Long-range correlation-induced effects at high-order harmonic generation on graphene quantum dots

H.K. Avetissian, A.G. Ghazaryan, Kh.V. Sedrakian, and G.F. Mkrtchian\*  
*Centre of Strong Fields Physics at Research Institute of Physics,  
Yerevan State University, Yerevan 0025, Armenia*

This paper focuses on investigating high-order harmonic generation (HHG) in graphene quantum dots (GQDs) under intense near-infrared laser fields. To model the GQD and its interaction with the laser field, we utilize a mean-field approach. Our analysis of the HHG power spectrum reveals fine structures and a noticeable enhancement in cutoff harmonics due to the long-range correlations. We also demonstrate the essential role of Coulomb interaction in determining of harmonics intensities and cutoff position. Unlike atomic HHG, where the cutoff energy is proportional to the pump wave intensity, in GQDs the cutoff energy scales with the square root of the field strength amplitude. A detailed time-frequency analysis of the entire range of HHG spectrum is presented using a wavelet transform. The analysis reveals intricate details of the spectral and temporal fine structures of HHG, offering insights into the various HHG mechanisms in GQDs.

## I. INTRODUCTION

After implementation of lasers, there has been a growing interest in designing and constructing novel materials with exceptional nonlinear optical properties, due to their potential applications in optoelectronics [1, 2] and nanophotonics [3, 4]. Along with the second and third perturbative harmonics [5], the extreme nonlinear response such as high-order harmonics generation [6] and wave mixing via nonlinear channels are already actual, which is of great importance in solving various contemporary problems. These include spectroscopy of attosecond resolution [7], generation of short wavelength coherent radiation [8], recovery of electronic [9] and topological properties of materials [10–12], observation of dynamical Bloch oscillations [13], Peierls [14] and Mott [15] transitions. Therefore, the design and development of new materials with unique nonlinear optical properties remains a highly active research field. Among the novel materials, the carbonbased nanomaterials, such as fullerenes [16, 17], carbon nanotubes [18], graphene [19], graphyne [20], graphdiyne [21] are widely used to design nonlinear optical materials. Carbon nanosystems are attractive for extreme nonlinear optics because of the presence of copious delocalized  $\pi$ -electrons in them. Graphene possessing extensive  $\pi$ -conjugation, shows extraordinary nonlinear properties [22]. Theoretical works predicted a strong HHG from fullerenes [23–27]. One of the possibilities to manipulate the optical properties of graphene-based materials is the further decreasing the dimensionality of the system to obtain graphene nanoribbon or zero dimensional GQD [28]. The phenomenon of HHG in graphene nanoribbons [29–31] and GQDs are also reported [32–35] and they found the change in nonlinear optical properties by varying the size, shape, and edges of these systems. The electronic properties of GQDs are close to atomic and molecular systems. However, because there

are only a limited number of levels, the HHG process cannot be adequately explained by the typical three-step model [36], where the continuum serves as the energy-acquiring location. Instead, the process exhibits similarities to HHG in atomic systems with the both permanent dipole moments [37, 38] and no dipole moments [39–45], where resonance and level dressing have a significant impact. In atomic systems with a limited number of levels, the cutoff frequency of HHG is not solely determined by the system’s intrinsic energy offset. Rather, it is influenced by transitions between numerous virtual states that are manipulated by the amplitude and frequency of the wave field, through the process of level dressing induced by the strong laser field [38, 45]. The successful model for the description of GQDs is the tight-binding (TB) one with various parametrizations. In the homogeneous electric field  $\mathbf{E}(t)$  according to Peierls substitution [46] the hopping integral  $t_{ij}$  acquire a phase  $(\mathbf{r}_i - \mathbf{r}_j) \cdot \int \mathbf{E}(t) dt$  upon electron tunneling from site  $\mathbf{r}_i$  to  $\mathbf{r}_j$ . In the mean-field approximation, the electron-electron interaction (EEI) alters hopping integrals and causes them to become non-zero between distant nodes, regardless of their separation. The Hansen-Bessel formula [47] suggests that a phase exhibiting large amplitude oscillations is equivalent to high harmonic oscillations of the effective hopping integrals. Therefore, in case of HHG in the strong fields, the second-next-nearest, third-next-nearest hopping, and long-range Coulomb interactions may all have a significant impact. It is worth noting that in graphene, the second-next-nearest hopping breaks electron-hole symmetry [48], which is important for a doped system. However, if one considers an undoped system and neglects thermal occupations, the HHG process is unaffected by the second-next-nearest hopping.

Theoretical analyses of HHG in GQD have so far focused on a free electron model with the next nearest hopping integral [35] and short-range Coulomb interactions only [32–34]. However, the question of influence of the long-range correlations on the HHG process and

\* mkrtchian@ysu.am

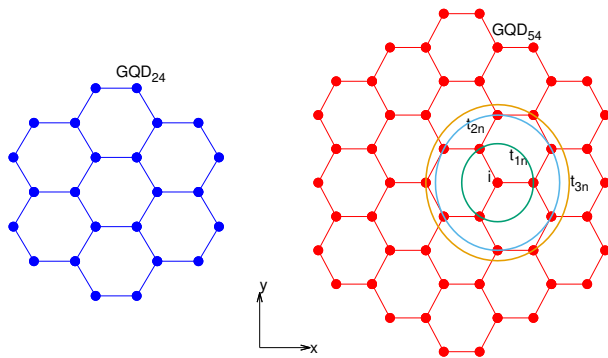


FIG. 1. Shown here are the schematic structures of GQD<sub>24</sub> and GQD<sub>54</sub>, which share the same point group as graphene. We also display the geometry used and highlight the nearest-neighbor (3 atoms), next-nearest-neighbor (6 atoms), and third nearest-neighbor (3 atoms) sites, along with their corresponding hopping integrals.

sub-cycle electronic response in these systems remains unclear. In this study, we develop a microscopic theory of GQD nonlinear interaction with the strong electromagnetic radiation that takes into account the long-range hopping integrals and EEI. Specifically, we investigate two GQDs, shown in Figure 1, with the same point group symmetry  $C_{6v}$  but differing in the number of atoms – GQD<sub>24</sub> and GQD<sub>54</sub>, allowing us to study size effects. Using the dynamical Hartree-Fock (HF) approximation, we uncover the general and fundamental structure of the HHG spectrum depending on the long-range parameters. Our investigations not only provide particular results for GQDs but also have the potential to be generalized to other systems within this family.

The paper is organized as follows. In Sec. II, the model and the basic equations are formulated. In Sec. III, we present the main results. Finally, conclusions are given in Sec. IV.

## II. THE MODEL AND THEORETICAL METHODS

We start by describing the model and theoretical approach. GQD is assumed to interact with a mid-infrared or visible light laser pulse that excites electron coherent dynamics. In particular, we consider the two versions of GQD. Both GQDs which deployed in Fig. 1 are invariant under the inversion with respect to the center of mass. We assume a neutral GQD, which will be described in the scope of the TB theory. Hence, the total Hamiltonian reads:

$$\hat{H} = \hat{H}_{\text{TB}} + \hat{H}_C + \hat{H}_{\text{int}}, \quad (1)$$

where

$$\hat{H}_{\text{TB}} = - \sum_{i,j\sigma} t_{ij} c_{i\sigma}^\dagger c_{j\sigma} \quad (2)$$

is the free GQD TB Hamiltonian. Here  $c_{i\sigma}^\dagger$  ( $c_{i\sigma}$ ) creates (annihilates) an electron with the spin polarization  $\sigma = \{\uparrow, \downarrow\}$  at the site  $i$  ( $\bar{\sigma}$  is the opposite to  $\sigma$  spin polarization). The hopping integral,  $t_{ij}$ , is taken up to third-nearest-neighbor. The overlap integrals and longer range interactions could also be included but they are expected to have minor effect on the process considered. For hopping integral we assume  $t_{1n} = 2.78$  eV for nearest-neighbor,  $t_{2n} = 0.12$  eV for next-nearest-neighbor, and  $t_{3n} = 0.068$  eV for third nearest-neighbor hopping [49]. The edges of the GQD are considered to be hydrogen passivated, which has little effect on the bonds.

The second term in the total Hamiltonian (1) describes the EEI. Within the HF approximation, the Hamiltonian  $\hat{H}_C$  is approximated by,

$$\begin{aligned} \hat{H}_C^{HF} = & U \sum_i (\bar{n}_{i\uparrow} - \bar{n}_{0i\uparrow}) n_{i\downarrow} \\ & + U \sum_i (\bar{n}_{i\downarrow} - \bar{n}_{0i\downarrow}) n_{i\uparrow} + \sum_{i,j} V_{ij} (\bar{n}_j - \bar{n}_{0j}) n_i \\ & - \sum_{i,j\sigma} V_{ij} c_{i\sigma}^\dagger c_{j\sigma} \left( \langle c_{i\sigma}^\dagger c_{j\sigma} \rangle - \langle c_{i\sigma}^\dagger c_{j\sigma} \rangle_0 \right), \quad (3) \end{aligned}$$

with on-site and inter-site Coulomb repulsion energies  $U$  and  $V_{ij}$ , respectively. The density operator is:  $n_{i\sigma} = c_{i\sigma}^\dagger c_{i\sigma}$ , and the total electron density for the site  $i$  is:  $n_i = n_{i\uparrow} + n_{i\downarrow}$ . Here  $\bar{n}_{i\sigma} = \langle c_{i\sigma}^\dagger c_{i\sigma} \rangle$  and  $\rho_{ji}^{(\sigma)} = \langle c_{i\sigma}^\dagger c_{j\sigma} \rangle$ . The Coulomb interaction matrix elements can be obtained from numerical calculations by using Slater  $\pi_z$  orbitals [28, 50]. Introducing an effective dielectric constant  $\epsilon$  which accounts for the substrate-induced screening in the 2D nanostructure, we take onsite interaction parameter as  $U = 16.5/\epsilon$  eV,  $V_{ij} = 8.6/\epsilon$  eV for nearest-neighbor,  $V_{ij} = 5.3/\epsilon$  eV for next-nearest-neighbor. The longer range Coulomb interaction is taken to be  $V_{ij} = 14.4/(\epsilon d_{ij})$  eV, where  $d_{ij}$  is the distance in angstrom between the distant neighbors. In Coulomb Hamiltonian Eq. (3) the exchange and scattering terms are neglected. The effective dielectric constant is taken to be  $\epsilon = 6$  [51]. Since in the TB Hamiltonian we assumed bulk graphene parameters in the Hartree-Fock Hamiltonian (3) we subtract the graphene bulk density matrix  $\rho_{0ji}^{(\sigma)} \equiv \langle c_{i\sigma}^\dagger c_{j\sigma} \rangle_0$  ( $\bar{n}_{0i\sigma} = \rho_{0ii}^{(\sigma)}$ ) already present in the TB term [28, 52].

The last term in the total Hamiltonian (1) is the light-matter interaction part that is described in the length-gauge via the pure scalar potential,

$$\hat{H}_{\text{int}} = e \sum_{i\sigma} \mathbf{r}_i \cdot \mathbf{E}(t) c_{i\sigma}^\dagger c_{i\sigma}, \quad (4)$$

with the elementary charge  $e$ , position vector  $\mathbf{r}_i$ , and the electric field strength  $\mathbf{E}(t) = f(t) E_0 \hat{\mathbf{e}} \cos \omega t$ , with the frequency  $\omega$ , polarization  $\hat{\mathbf{e}}$  unit vector, and amplitude  $E_0$ . The wave envelope is described by the Gaussian function  $f(t) = \exp[-2 \ln 2 (t - t_m)^2 / \mathcal{T}^2]$ , where  $\mathcal{T}$  characterizes the pulse duration full width at half maximum,  $t_m$  defines the position of the pulse maximum. Note that for the Gaussian envelope the number of oscillations  $N_s$  of the field is approximated as  $\mathcal{T}/T \simeq 0.307 N_s$ , where  $T = 2\pi/\omega$  is the wave period.

From the Heisenberg equation we obtain evolutionary equations for the single-particle density matrix  $\rho_{ij}^{(\sigma)} = \langle c_{j\sigma}^\dagger c_{i\sigma} \rangle$ :

$$i\hbar \frac{\partial \rho_{ij}^{(\sigma)}}{\partial t} = \sum_k \left( \tau_{kj\sigma} \rho_{ik}^{(\sigma)} - \tau_{ik\sigma} \rho_{kj}^{(\sigma)} \right) + (V_{i\sigma} - V_{j\sigma}) \rho_{ij}^{(\sigma)} + e\mathbf{E}(t) \cdot (\mathbf{r}_i - \mathbf{r}_j) \rho_{ij}^{(\sigma)} - i\hbar\gamma \left( \rho_{ij}^{(\sigma)} - \rho_{eij}^{(\sigma)} \right), \quad (5)$$

where

$$V_{i\sigma} = \sum_{j\alpha} V_{ij} \left( \rho_{jj}^{(\alpha)} - \rho_{0jj}^{(\alpha)} \right) + U \left( \rho_{ii}^{(\bar{\sigma})} - \rho_{0ii}^{(\bar{\sigma})} \right), \quad (6)$$

and

$$\tau_{ij\sigma} = t_{ij} + V_{ij} \left( \rho_{ji}^{(\sigma)} - \rho_{0ji}^{(\sigma)} \right) \quad (7)$$

are defined via the density matrix  $\rho_{ij}^{(\sigma)}$  and Coulomb terms. As we see due to the mean field modification hopping integrals become non-zero between the remote nodes, irrespective of the distance.

In the Hartree-Fock or mean-field approximation, the higher order correlation terms are neglected. Calculating the dynamics of the correlation terms (in the second Born approximation) allows the investigation of scattering processes which have been introduced in Eq. (5) phenomenologically via damping term, assuming that the system relaxes at a rate  $\gamma$  to the equilibrium  $\rho_{eij}^{(\sigma)}$  distribution. Optically excited electrons undergo relaxation processes towards equilibrium through various scattering mechanisms, which include interactions such as electron-phonon, electron-electron, or electron-impurity scattering. In the case of graphene-like nanostructures, both experimental investigations [53, 54] and theoretical analyses [55, 56] indicate that the predominant influence on relaxation dynamics arises from electron-electron scatterings characterized by timescales typically on the order of tens of femtoseconds. In the context of GQDs, the relaxation rates can be even more pronounced due to the reduction in dynamic screening effects. Therefore, in the present study, we have established a relaxation rate of  $\hbar\gamma = 0.2$  eV.

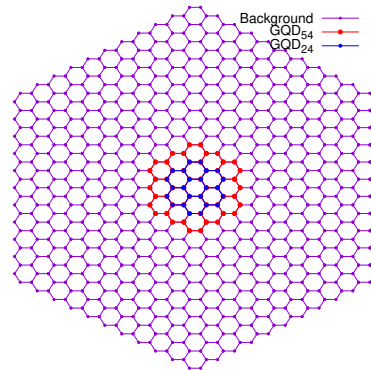


FIG. 2. To determine the bulk density matrix, we employ GQD<sub>726</sub> and position the reference GQDs at its center. The density matrix elements of GQD<sub>726</sub> are utilized as a bulk in the Hartree-Fock Hamiltonian (3).

### III. RESULTS

After the outlining theoretical setup, we begin by examining the HF quasi-particle spectrum, which is characterized by a fully occupied valence band and a completely empty conduction band. The eigenstates and eigenenergies of the systems under consideration prior to interaction with a strong laser pulse can be determined self-consistently by iterating Eq. (3). To calculate the bulk density matrix, we use a sufficiently large GQD and place reference GQDs in the middle, as shown in Fig. 2. This approach allows us to obtain the necessary bulk density matrix elements for the reference GQDs, which are not influenced by boundary effects. With the help of the obtained eigenstates  $\psi_\mu(i)$  we also calculate the matrix elements of the transition dipole moment:

$$\mathbf{d}_{\mu'\mu} = e \sum_i \psi_{\mu'}^*(i) \mathbf{r}_i \psi_\mu(i). \quad (8)$$

Beginning the iteration with TB orbitals, the converged results are presented in Figs. 3 and 4. Intraband and interband transitions in GQD<sub>24</sub> and GQD<sub>54</sub> are analyzed in terms of the energy-difference dependence of the absolute values of transition dipole moment's matrix elements in Fig. 3. As is seen from Fig. 3, the Coulomb interaction shifts transitions peaks to higher energies, that is oscillator strengths at higher energies have relatively larger weight than in the case of free electrons. This effect is due to the fact that the long range Coulomb interactions give rise to large hopping integrals between the remote nodes (7) in the HF approximation. Eigenenergies with and without EEI for GQD<sub>24</sub> and GQD<sub>54</sub> are presented in Figs. (4a) and (4b), respectively, demonstrating the effect of EEI on the system's energy spectrum. Compared with the GQD<sub>24</sub>, the GQD<sub>54</sub> has more nearly degenerated states, and as a consequence, more channels for the interband and intraband transitions.

The HHG spectrum is obtained by taking the Fourier

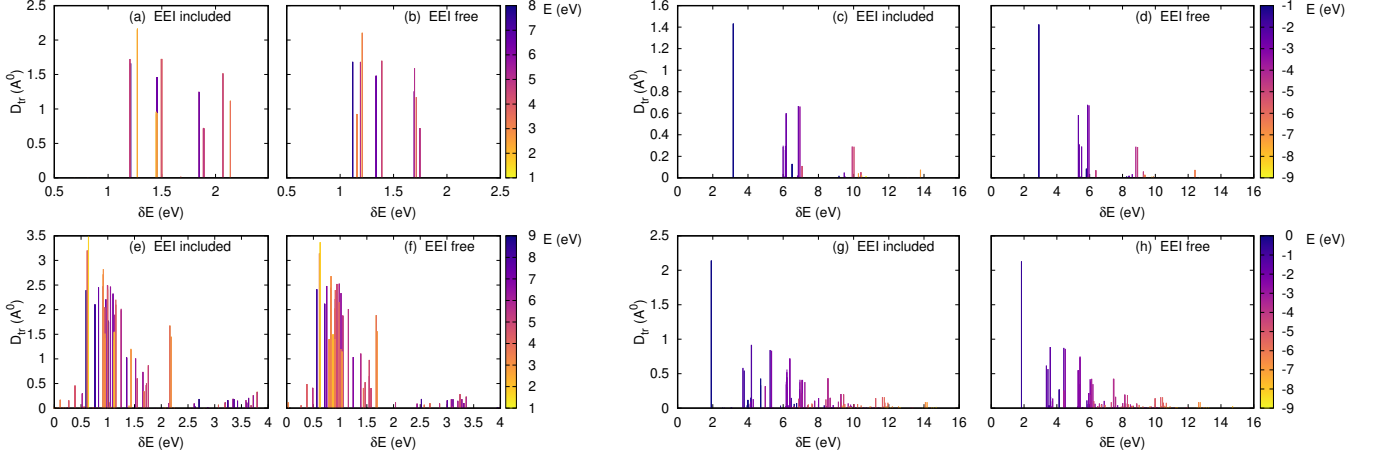


FIG. 3. Absolute values of transition dipole moment matrix elements are presented for GQD<sub>24</sub> (a, b, c, d) and GQD<sub>54</sub> (e, f, g, h), showing the energy dependence of intraband (a, b, e, f) and interband transitions (c, d, g, h), with and without EEI. For intraband transitions it is shown only conduction band, since similar picture we have for valence band. The color boxes show energy ranges of the corresponding bands.

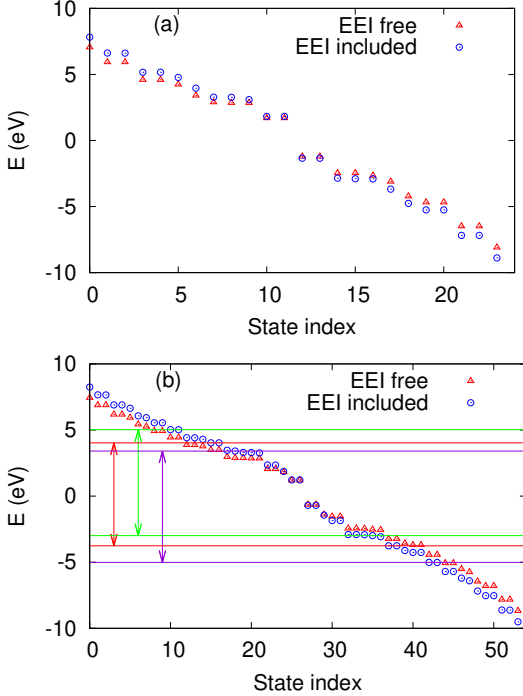


FIG. 4. Eigenenergies with and without EEI for GQD<sub>24</sub> and GQD<sub>54</sub> are presented in (a) and (b), respectively. In (b) it is shown also resonant levels with corresponding transitions responsible for five photon resonance.

transform  $\mathbf{a}(\Omega)$  of the dipole acceleration  $\mathbf{a}(t) = d^2\mathbf{d}/dt^2$ , where the dipole moment is defined as

$$\mathbf{d}(t) = e \sum_{i\sigma} \mathbf{r}_i \rho_{ii}^{(\sigma)}(t). \quad (9)$$

Although we perform our calculations in the coordinate basis, for physical insight it is useful to consider also

the dynamics in the energetic representation where there are two contributions to the dipole moment: the transitions of electrons/holes within conduction and valence bands, and the creation of electron-hole pairs (transitions from occupied molecular orbitals to unoccupied ones) followed by their recombination. To distinguish intraband and interband contributions within the dipole acceleration spectrum, we need to perform a basis transformation using the formula:

$$\rho_{ij} = \sum_{\mu'} \sum_{\mu} \psi_{\mu'}^*(j) \varrho_{\mu\mu'} \psi_{\mu}(i), \quad (10)$$

where  $\psi_{\mu}(i)$  represents the Hartree-Fock orbitals, and  $\rho_{\mu\mu'}$  is the density matrix in the energetic representation. The inverse transformation is given by:  $\varrho_{\mu\mu'} = \sum_i \sum_j \psi_{\mu}^*(i) \rho_{ij} \psi_{\mu'}(j)$ . Since our consideration does not involve spin effects, we omit the spin index and multiply our results by the degeneracy factor of 2. In this representation  $\varrho_{\mu\mu}$  is the population of state with energy  $\varepsilon_{\mu}$ , while nondiagonal elements of the density matrix  $\varrho_{\mu\mu'}$  characterize coupling of levels (i.e., the appearance of coherence). Using Eqs. (8) and (10), we can express the dipole moment (9) as:

$$\mathbf{d}(t) = \mathbf{d}_{\text{intra}}(t) + \mathbf{d}_{\text{inter}}(t), \quad (11)$$

where

$$\mathbf{d}_{\text{intra}}(t) = 2 \sum_{\mu, \mu'=N/2}^{N-1} \varrho_{\mu\mu'}(t) \mathbf{d}_{\mu'\mu} + 2 \sum_{\mu, \mu=0}^{N/2-1} \varrho_{\mu\mu'}(t) \mathbf{d}_{\mu'\mu}, \quad (12)$$

represents the intraband part of the dipole moment, and

$$\mathbf{d}_{\text{inter}}(t) = 2 \sum_{\mu'=N/2}^{N-1} \sum_{\mu=0}^{N/2-1} \varrho_{\mu\mu'}(t) \mathbf{d}_{\mu'\mu} + \text{c.c.}, \quad (13)$$

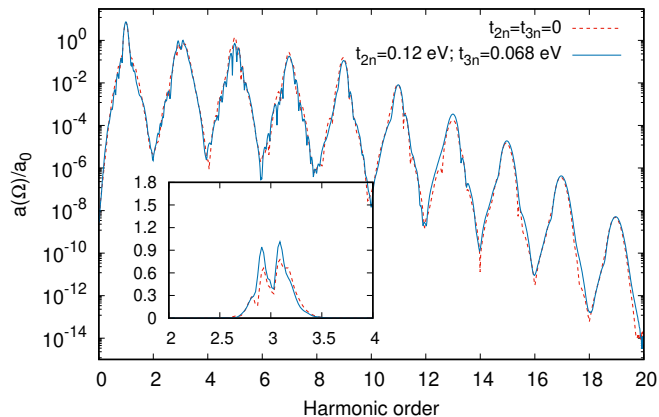


FIG. 5. The HHG spectra for GQD<sub>54</sub> in logarithmic scale via the normalized dipole acceleration Fourier transformation  $a(\Omega)/a_0$  (in arbitrary units) with and without long-range hopping integrals. The wave amplitude is taken to be  $E_0 = 0.5$  V/Å. The inset shows HHG spectra in the linear scale near the 3rd harmonic. The EEI is switched off.

represents the interband part. We preferred for calculations in the coordinate basis due to computational efficiency that is approximately one order of magnitude faster than in the energetic representation.

To compute the harmonic signal, we use the Fourier transform

$$\mathbf{a}(\Omega) = \int_0^{\mathcal{T}} \mathbf{a}(t) e^{i\Omega t} W(t) dt,$$

where  $W(t)$  is a window function that suppresses small fluctuations and reduces the overall background noise of the harmonic signal [57]. We choose the pulse envelope  $f(t)$  as the window function. The excitation is performed using a Ti:sapphire laser with a wavelength of 780 nm, an excitation frequency of  $\omega = 1.59$  eV/ $\hbar$ , which is comparable to the gaps of GQD<sub>24</sub> (3.16 eV) and GQD<sub>54</sub> (1.92 eV). For all further calculations we assume that the wave is linearly polarized with a polarization unit vector  $\hat{\mathbf{e}} = \{1, 0\}$ , and the pulse duration  $\mathcal{T}$  is set to 20 fs, corresponding to approximately 25 oscillations ( $N_s \simeq 25$ ). To ensure a smooth turn-on of the interaction, we position the pulse center at  $t_m = 25T$ . For convenience, we normalize the dipole acceleration by the factor  $a_0 = e\bar{\omega}^2\bar{d}$ , where  $\bar{\omega} = 1$  eV/ $\hbar$  and  $\bar{d} = 1$  Å. The power radiated at a given frequency is proportional to  $\mathbf{a}^2(\Omega)$ . We perform the time integration of Eq. (5) using the eighth-order Runge-Kutta algorithm.

To begin with, we examine the effect of the next-nearest-neighbor and third-nearest-neighbor hopping integrals on the HHG spectra, with the EEI turned off for simplicity. Figure 5 illustrates a comparison of the relative HHG spectra for GQD<sub>54</sub> with and without long-range hopping integrals. It is evident from this figure that the long-range hopping integrals have a measurable impact on the HHG spectra. This influence is more pronounced in the linear scale, as shown in the inset for the

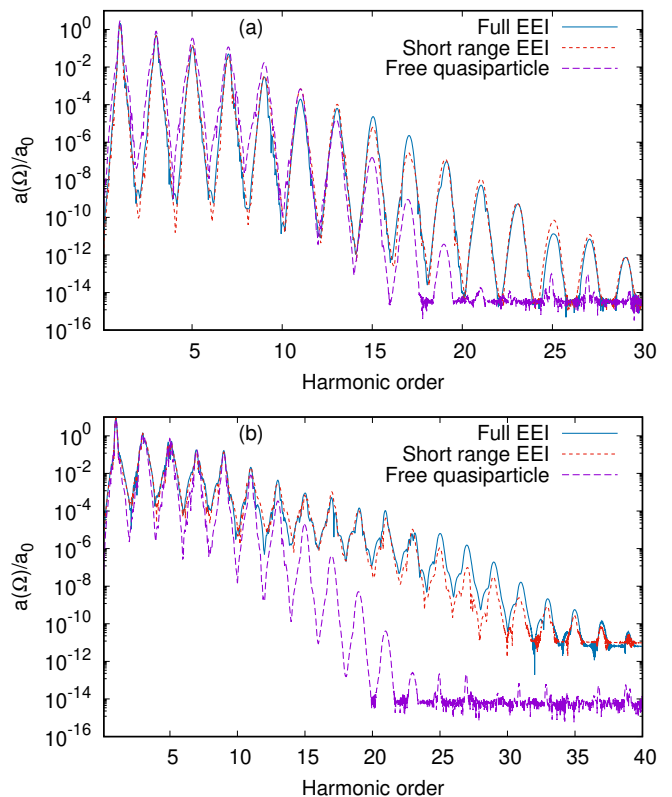


FIG. 6. The relative HHG spectra for GQD<sub>24</sub> (a) and for GQD<sub>54</sub> (b) via the normalized dipole acceleration Fourier transformation  $a(\Omega)/a_0$  with and without EEI. The wave amplitude is taken to be  $E_0 = 0.5$  V/Å.

3rd harmonic, where we observe a difference of up to 50%.

Then, we will examine the impact of Coulomb interaction on the HHG spectra. The HHG spectra are compared for three different scenarios in Fig. 6: when the full Coulomb effects are considered, when the long-range Coulomb interaction is eliminated, and when there are no Coulomb effects present, and the quasiparticles are free. The inclusion of the Coulomb interaction leads to several noteworthy characteristics in the HHG spectra: (a) the most prominent feature is a substantial increase in the HHG signal by several orders of magnitude in the mid-plateau and near the cutoff regime compared to the case of free quasiparticles. (b) The cutoff frequency is significantly enhanced. (c) In the vicinity of the cutoff regime, the spectra are distinguished by featureless peaks, while for low harmonics there is a multiple-peak splitting pattern in each main harmonic peak. These fine structures are entirely reproducible and convey crucial information about the electron quantum dynamics and the underlying mechanism which will be discussed later. To observe the effects of the EEI on HHG process in an actual experiment, it is essential to have the ability to manipulate the strength of the Coulomb interaction. In most experimental setups, graphene nanostructures are situated on



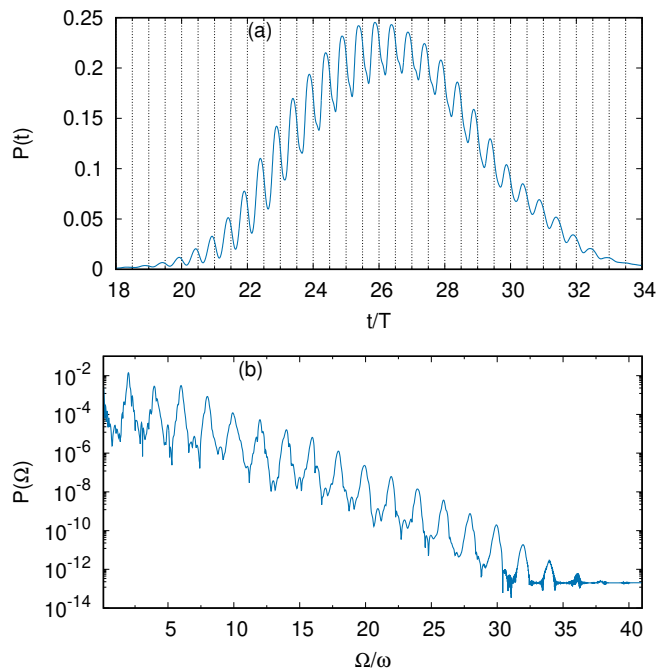


FIG. 7. (a) Population of the state with an energy of 2.34 eV versus time (optical cycles) for GQD<sub>54</sub> and its Fourier transform (b). Laser parameters same as those in Fig. 5.

a substrate, which introduces a screening effect on the Coulomb interaction, typically reducing it to about  $1/\epsilon$  of its original strength, where  $\epsilon$  represents the substrate's dielectric constant. Specifically, when using a substrate like SiO<sub>2</sub>, the Coulomb interaction remains moderate. However, by introducing substrates in contact with liquids of high dielectric constant, like ethanol ( $\epsilon \approx 13$ ), it is possible to significantly enhance the background dielectric constant. Consequently, in the experiment, one can vary  $\epsilon$ , thereby tuning the Coulomb interaction to investigate its impact on HHG process in GQDs.

The significant enhancement in the HHG signal can be explained by the strong modification of hopping integrals (7) and the resulting level dressing (as shown in Fig. 7) due to the mean field effect. This is supported by the observation that when the long-range Coulomb interaction is turned off, the effect is weakened, and these features are more noticeable in GQD<sub>54</sub>. Another indication is that the maximum harmonic order generated through transitions between the real energy levels, as clear from Fig. 4, is only up to the 9th order, while the enhancement occurs in higher harmonics generated through transitions between the virtual levels. As an example, Fig. 7 illustrates the population of the state with an energy of 2.34 eV as a function of time and its Fourier transform. It is evident from the figure that there are rapid oscillations in the level populations that include high harmonics of the fundamental frequency.

Another notable aspect of the HHG signals in GQDs is their dependence on the size of the dot. The HHG sig-

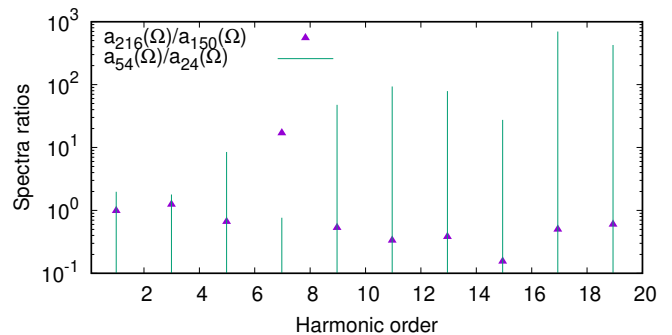


FIG. 8. The ratio of HHG signals per particle for GQD<sub>54</sub> to that for GQD<sub>24</sub>, using the same laser parameters as in Figure 5. By the triangles it is shown the ratio of HHG signal per particle for GQD<sub>216</sub> to that for GQD<sub>150</sub>.

nals per particle for GQD<sub>24</sub> and GQD<sub>54</sub> are compared in Fig. 8. As demonstrated, there is a significant increase in the HHG signal for GQD<sub>54</sub>, a result also observed for triangular GQDs according to previous studies [32]. This enhancement may be attributed to the density of states, which is indirectly reflected in Fig. 3 via the transition dipole moments. This figure reveals that GQD<sub>54</sub> has substantially more transition channels than GQD<sub>24</sub>. As the size of the dot increases, this effect reaches saturation [32]. We have made also calculations for larger dots – GQD<sub>150</sub> and GQD<sub>216</sub> and compared the spectra in the Fig. 8. As is seen, already for GQD<sub>150</sub> the overall enhancement of HHG yield per particle due to the size of the dot is absent.

To investigate the underlying causes of the detailed spectral structures observed in the HHG spectra Fig. 6, we utilize a wavelet transform [58] of the dipole acceleration to conduct a time-frequency analysis. We perform the Morlet transform ( $\sigma = 20$ ) of the dipole acceleration:

$$\mathbf{a}(t, \Omega) = \sqrt{\frac{\Omega}{\sigma}} \int_0^\tau dt' \mathbf{a}(t') e^{i\Omega(t'-t)} e^{-\frac{\Omega^2}{2\sigma^2}(t'-t)^2}. \quad (14)$$

The wavelet transform of the dipole acceleration provides insight into the origin of the HHG spectral fine structures. Figure 9 illustrates the absolute values of the time-frequency profiles of the dipole acceleration, which have been obtained using the laser parameters presented in Fig. 6 for GQD<sub>54</sub>. This plot shows remarkable details of the spectral and temporal structures. Notably, the time profiles for the low harmonics Fig. 9(a) exhibit a fairly smooth variation with respect to time for a given frequency. Conversely, for high harmonics near the cutoff region Fig. 9(b), the most distinct feature is the rapid-burst time profiles. These bursts occur with a period of  $0.5T$ , which supports the level dressing model of HHG, since the time profile resembles the population behavior depicted in Fig. 7. As an example, the time profile of the harmonic (H23) is represented in Fig. 10. It demonstrates the occurrence of two bursts during the each optical cycle.

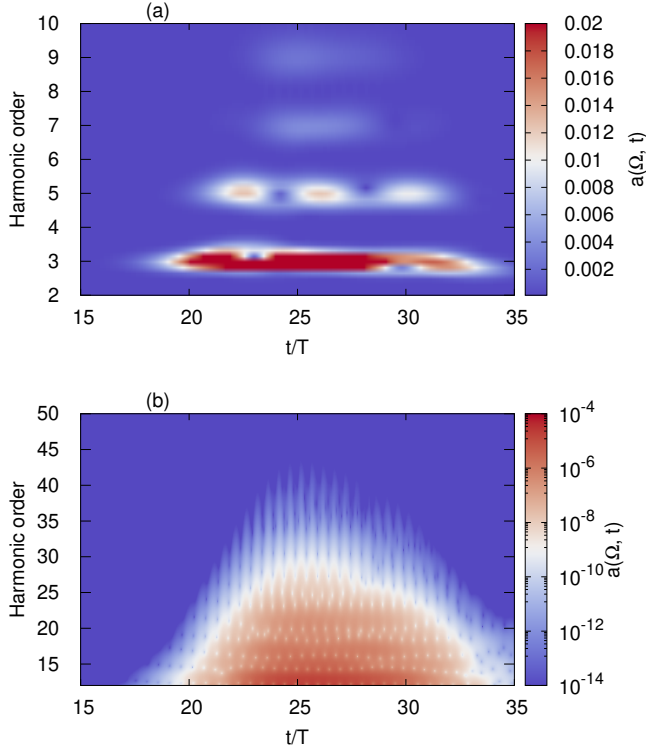


FIG. 9. The spectrogram (color box in arbitrary units) of the HHG process via the wavelet transform of the dipole acceleration for GQD<sub>54</sub>: (a) for the low harmonics and (b) for the high harmonics. It is shown  $|a(t, \Omega)|$  in a time interval where the wave's amplitude is considerable. The laser parameters correspond to Fig. 6. The similar picture we have for GQD<sub>24</sub>.

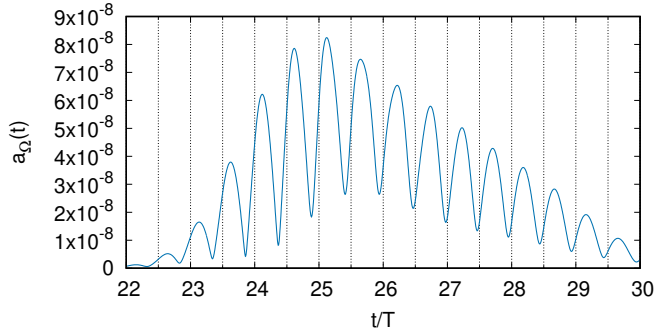


FIG. 10. The time profile of the 23rd harmonic of GQD<sub>54</sub>, obtained from cross sections of the time-frequency spectrum in Fig. 9(b).

Moving on, we will now discuss the multiple-peak splitting patterns observed for the low harmonics. Figure 11 presents the HHG spectrum of GQD<sub>54</sub>, highlighting the detailed fine structure of the peaks near the 3rd ( $\hbar\Omega \simeq 4.8$  eV) and 5th harmonics ( $\hbar\Omega \simeq 8$  eV). When we examine Fig. 3(g), we observe that the dipole moments for interband transitions have peaks around these frequencies, indicating the possibility of multiphoton resonant

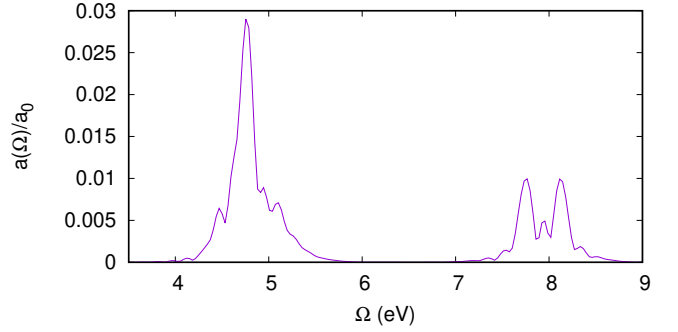


FIG. 11. The HHG spectrum of GQD<sub>54</sub> is presented in the linear scale in the vicinity of the 3rd and 5th harmonics, showcasing the intricate fine structure of the peaks. The laser parameters used in this analysis correspond to those presented in Figure 6.

transitions. The sidebands near the 3rd and 5th harmonics correspond to these resonant transitions. This is further supported by the time profiles obtained from cross sections of the time-frequency spectrum in Fig. 9(a) around these frequencies. The results for the 3rd and 5th harmonics are presented in Figures 12 and 13, respectively. In Fig. 12, the profiles for the 3rd harmonic and the two sidebands exhibit striking differences, suggesting distinct mechanisms for their generation. The time profile of the 3rd harmonic closely follows the envelope of the laser pulse, with only minor modifications attributed to nearby resonances. In contrast, the time profiles of the sidebands exhibit a relatively flat behavior, indicating their origin in multiphoton resonant bound-bound transitions. For nearly resonant transitions, the product  $e^{in\omega t} \rho_{\mu\mu'}(t)$ , which defines time profile of the  $n$ th harmonic according to Eq. (13), has a non-zero average value over the course of a laser cycle, and it varies slowly within the time frame of that cycle. Consequently, this leads to the observed flat time profiles of the sidebands. In the presence of strong laser fields, one should also take into account the dynamic Stark shifts of energy levels  $S_\mu(t)$ , which may become crucial [59]. These shifts, which are proportional to the laser intensity profile  $E_0^2 f^2(t)$ , have the capability to adjust otherwise non-resonant energy levels into resonance conditions, i.e.,  $\varepsilon_\mu + S_\mu(t) - \varepsilon_{\mu'} - S_{\mu'}(t) \approx n\omega$  or vice versa. In the context of the five-photon resonance transitions illustrated in Fig. 4(b), this situation arises with three pairs of nearly resonant transitions subjected to dynamic Stark shift. The time profile of the resulting triple structure near the 5th harmonic (as shown in Fig. 13) distinctly displays oscillations occurring approximately every five optical cycles. This effect is due to the fact that throughout the interaction of GQDs with the laser field, populations from valence band states are transferred to excited conduction band states via dynamic Stark-shifted resonances. These resonances can emerge multiple times during the pulse [60], as the dynamic Stark shift can be either positive

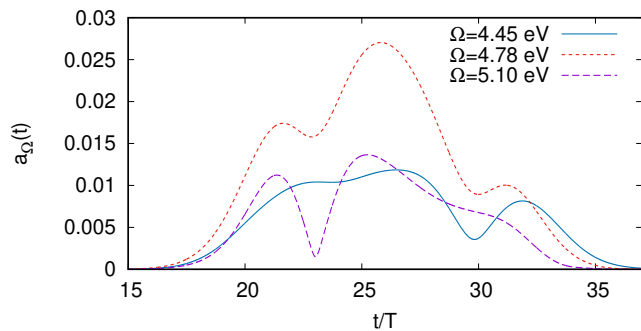


FIG. 12. The time profiles of the 3rd harmonic and sidebands. Laser parameters are the same as those in Fig. 9.

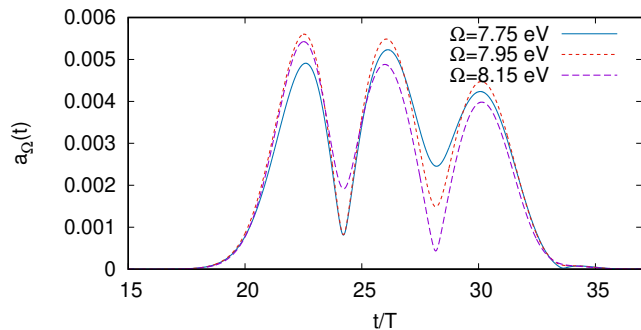


FIG. 13. The time profiles of the triple structure near the 5th harmonic. Laser parameters are the same as those in Fig. 9.

or negative, depending on the specific energy state. Notably, the peaks in the time profile of the 5th harmonic correspond to the peaks of levels' coherence  $\rho_{\mu\mu'}(t)$ . It should be noted that in the midplateau domain of harmonics, we have interplay between the intraband (12) and interband (13) emissions.

Next we investigate the dependence of cutoff frequency on the pump wave intensity by analyzing the HHG spectra for the different intensities. The dependence of the HHG spectra on the wave field amplitude for both GQDs is shown in Fig. 14. A significant nonlinear dependence of the mid-plateau and near-cutoff harmonics on the pump wave amplitude is observed in Fig. 14. In addition, unlike atomic HHG [36], where the cutoff energy is proportional to the square of the field strength amplitude, the cutoff energy in our case scales with the square root of the field strength amplitude. This trend becomes evident when observing the inset in the lower panel of Figure 14, wherein we depict the relationship between the cutoff harmonics and the wave field amplitude ( $E_0$ ). The plotted data is accompanied by a fitting function of the form  $\sqrt{E_0}$ . Within the range of field strengths spanning up to  $0.8 \text{ V/\AA}$ , a remarkable alignment between the data and the scaling function is observed, indicative of a strong approximation. Nevertheless, it's noteworthy that a saturation phenomenon becomes apparent for higher intensity pump waves.

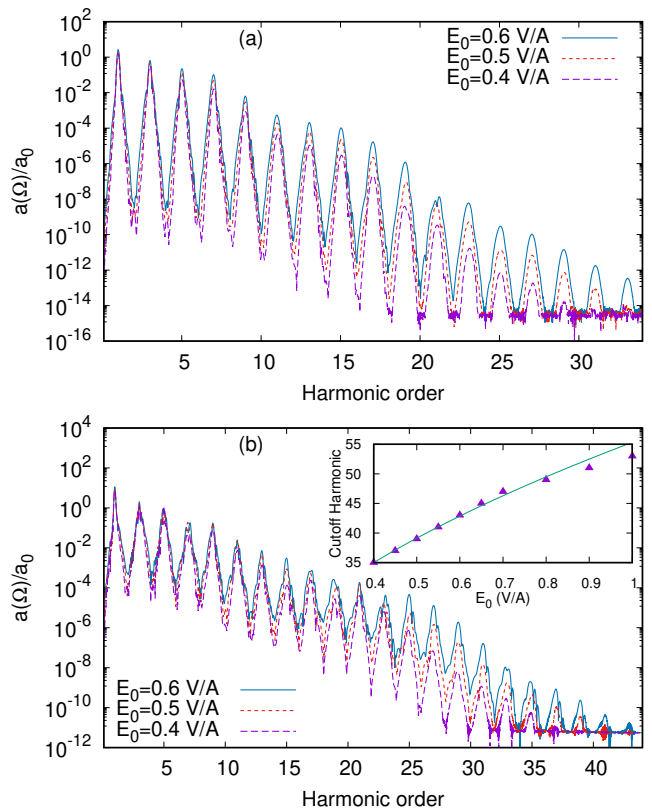


FIG. 14. The dependencies of the HHG spectra on the wave field amplitude are illustrated GQD<sub>24</sub> (a) and for GQD<sub>54</sub> (b) using the normalized dipole acceleration Fourier transformation,  $a(\Omega)/a_0$ , plotted on a logarithmic scale. The inset in (b) shows the dependence of cutoff harmonic on the wave field amplitude. The solid line is a fitting function of the form  $\sqrt{E_0}$ .

In the context of the experimental realization of HHG in GQDs, it's crucial to account for the arrangement of GQDs randomly distributed across the 2D surface. The angle, denoted as  $\theta$ , between one side of the hexagon (see Fig. 1) and the polarization vector of the incident wave plays a main role in determining the resulting HHG spectra. Therefore, it becomes necessary to consider a range of randomly distributed  $\theta$  values and subsequently perform averaging over these angles. Taking into consideration the symmetry inherent to the GQDs, we performed calculations with 100 randomly distributed  $\theta$  values spanning the range from 0 to  $\pi/3$  and then averaged the results. The results of this averaged HHG spectrum, in addition to the spectrum obtained at  $\theta = 0$ , are presented in Figure 15. Note that for a single GQD when  $\theta \neq 0$  there is also HHG in the perpendicular to laser polarization direction, which is averaged to zero. As depicted, the averaged HHG spectrum exhibits a reduction when compared to the optimal value at  $\theta = 0$ . Nonetheless, thanks to the high symmetry inherent in the considered GQD, this reduction does not have a critical impact on the overall result.



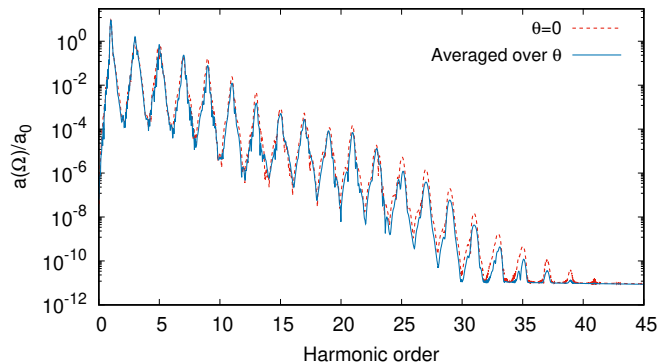


FIG. 15. The averaged HHG spectrum for GQD<sub>54</sub>. The averaging is performed over hexagon rotation angle with respect to wave polarization direction. The wave amplitude is taken to be  $E_0 = 0.5 \text{ V/\AA}$ .

#### IV. CONCLUSION

We have presented a comprehensive investigation into the extreme nonlinear optical response of the hexagonal graphene-based quantum dots. Specifically, we focused on GQDs composed of 24 and 54 carbon atoms, which represent inversion symmetric configurations commonly found in these systems. Our study employed an accurate quantal calculation of the HHG spectra using a mean-field approach that accounts for many-body Coulomb interaction. By solving the evolutionary equations for the single-particle density matrix, we disclosed intricate fine structures within the HHG spectra and observed a significant enhancement in mid-plateau and near-cutoff harmonics, which can be attributed to the effect of the long-range correlations. Our findings highlight the crucial role of the Coulomb interaction in determining of the harmon-

ics intensities and the cutoff position. To gain deeper insights into the high-harmonic generation mechanisms across the different energy ranges, we employed a detailed wavelet time-frequency analysis. Such analysis uncovered intricate spectral and temporal fine structures, shedding new light on the underlying processes involved. Additionally, our investigation revealed a strong dependence of the HHG spectra on the number of particles, indicating a preference for GQDs with a larger number of particles. While our results are presented for hexagonal GQDs, it is reasonable to expect similar outcomes for experimentally accessible GQDs with triangular and rectangular shapes, since the obtained results do not rely on the shape of the GQD. This broadens the applicability of our findings. Overall, our study provides a basic insight into the nonlinear optical response of GQDs and contributes to a better understanding of characteristics of such a significant phenomenon as HHG. However, it's important to note that our approach relied on TB theory, which includes several free parameters adjusted with respect to infinite graphene sheet. While this TB-based approach has provided valuable insights into GQD dynamics and their response to laser fields, we recognize that for a more detailed and precise description of the system's behavior, a more advanced method, such as time-dependent density functional theory (TDDFT), is required. In our future work, we plan to perform calculations within the framework of TDDFT. This approach will allow us to account for higher-order correlations without the need for adjustable parameters, leading to a more comprehensive understanding of GQD dynamics and their nonlinear optical response.

#### ACKNOWLEDGMENTS

The work was supported by the Science Committee of Republic of Armenia, project No.21AG-1C014.

- 
- [1] E. Rosencher and B. Vinter, *Optoelectronics* (Cambridge University Press, 2002).
  - [2] M. Grundmann, *Nano-optoelectronics: concepts, physics and devices* (Springer Science & Business Media, 2002).
  - [3] P. N. Prasad, *Nanophotonics* (John Wiley & Sons, 2004).
  - [4] F. Bonaccorso, Z. Sun, T. Hasan, and A. Ferrari, *Nature Photonics* **4**, 611 (2010).
  - [5] R. W. Boyd, *Nonlinear optics* (Academic press, 2020).
  - [6] P. B. Corkum, *Phys. Rev. Lett.* **71**, 1994 (1993).
  - [7] F. Krausz and M. Ivanov, *Rev. Mod. Phys.* **81**, 163 (2009).
  - [8] H. K. Avetissian, *Relativistic Nonlinear Electrodynamics: The QED Vacuum and Matter in Super-Strong Radiation Fields*, Vol. 88 (Springer, 2015).
  - [9] G. Vampa, T. J. Hammond, N. Thiré, B. E. Schmidt, F. Légaré, C. R. McDonald, T. Brabec, D. D. Klug, and P. B. Corkum, *Phys. Rev. Lett.* **115**, 193603 (2015).
  - [10] T. T. Luu and H. J. Wörner, *Nature Communications* **9**, 916 (2018).
  - [11] H. K. Avetissian and G. F. Mkrtchian, *Phys. Rev. B* **102**, 245422 (2020).
  - [12] H. K. Avetissian, V. N. Avetisyan, B. R. Avchyan, and G. F. Mkrtchian, *Phys. Rev. A* **106**, 033107 (2022).
  - [13] T. T. Luu, M. Garg, S. Y. Kruchinin, A. Moulet, M. T. Hassan, and E. Goulielmakis, *Nature* **521**, 498 (2015).
  - [14] D. Bauer and K. K. Hansen, *Phys. Rev. Lett.* **120**, 177401 (2018).
  - [15] R. Silva, I. V. Blinov, A. N. Rubtsov, O. Smirnova, and M. Ivanov, *Nature Photonics* **12**, 266 (2018).
  - [16] H. W. Kroto, J. R. Heath, S. C. O'Brien, R. F. Curl, and R. E. Smalley, *Nature* **318**, 162 (1985).
  - [17] P. W. Fowler and D. E. Manolopoulos, *An atlas of fullerenes* (Courier Corporation, 2007).
  - [18] S. Iijima, *Nature* **354**, 56 (1991).
  - [19] A. K. Geim, *Science* **324**, 1530 (2009).

- [20] Q. Peng, A. K. Dearden, J. Crean, L. Han, S. Liu, X. Wen, and S. De, *Nanotechnology, science and applications*, 1 (2014).
- [21] Y. Li, L. Xu, H. Liu, and Y. Li, *Chemical Society Reviews* **43**, 2572 (2014).
- [22] H. K. Avetissian, G. F. Mkrtchian, and A. Knorr, *Phys. Rev. B* **105**, 195405 (2022).
- [23] G. P. Zhang, *Phys. Rev. Lett.* **95**, 047401 (2005).
- [24] G. P. Zhang and T. F. George, *Phys. Rev. A* **74**, 023811 (2006).
- [25] G. P. Zhang and Y. H. Bai, *Phys. Rev. B* **101**, 081412(R) (2020).
- [26] H. K. Avetissian, A. G. Ghazaryan, and G. F. Mkrtchian, *Phys. Rev. B* **104**, 125436 (2021).
- [27] H. K. Avetissian, S. Sukiasyan, H. H. Matevosyan, and G. F. Mkrtchian, *Results Phys.* **53**, 106951 (2023).
- [28] A. D. Güçlü, P. Potasz, M. Korkusinski, P. Hawrylak, *et al.*, *Graphene quantum dots* (Springer, 2014).
- [29] J. D. Cox, A. Marini, and F. J. G. De Abajo, *Nature Communications* **8**, 14380 (2017).
- [30] H. K. Avetissian, B. R. Avchyan, G. F. Mkrtchian, and K. A. Sargsyan, *J. Nanophotonics* **14**, 026018 (2020).
- [31] X. Zhang, T. Zhu, H. Du, H.-G. Luo, J. van den Brink, and R. Ray, *Phys. Rev. Research* **4**, 033026 (2022).
- [32] B. Avchyan, A. Ghazaryan, K. Sargsyan, and K. V. Sedrakian, *Journal of Experimental and Theoretical Physics* **134**, 125 (2022).
- [33] B. R. Avchyan, A. G. Ghazaryan, S. S. Israelyan, and K. V. Sedrakian, *J. Nanophotonics* **16**, 036001 (2022).
- [34] B. Avchyan, A. Ghazaryan, K. Sargsyan, and K. V. Sedrakian, *JETP Letters* **116**, 428 (2022).
- [35] S. Gnawali, R. Ghimire, K. R. Magar, S. J. Hossaini, and V. Apalkov, *Phys. Rev. B* **106**, 075149 (2022).
- [36] M. Lewenstein, P. Balcou, M. Y. Ivanov, A. LHuillier, and P. B. Corkum, *Phys. Rev. A* **49**, 2117 (1994).
- [37] H. K. Avetissian, B. R. Avchyan, and G. F. Mkrtchian, *Phys. Rev. A* **77**, 023409 (2008).
- [38] H. K. Avetissian, B. R. Avchyan, and G. F. Mkrtchian, *Journal of Physics B: Atomic, Molecular and Optical Physics* **45**, 025402 (2011).
- [39] B. Sundaram and P. W. Milonni, *Phys. Rev. A* **41**, 6571 (1990).
- [40] L. Plaja and L. Roso-Franco, *JOSA B* **9**, 2210 (1992).
- [41] D. G. Lappas, M. V. Fedorov, and J. H. Eberly, *Phys. Rev. A* **47**, 1327 (1993).
- [42] A. E. Kaplan and P. L. Shkolnikov, *Phys. Rev. A* **49**, 1275 (1994).
- [43] F. I. Gauthey, C. H. Keitel, P. L. Knight, and A. Maquet, *Phys. Rev. A* **52**, 525 (1995).
- [44] S. De Luca and E. Fiordilino, *Journal of Physics B: Atomic, Molecular and Optical Physics* **29**, 3277 (1996).
- [45] F. I. Gauthey, B. M. Garraway, and P. L. Knight, *Phys. Rev. A* **56**, 3093 (1997).
- [46] R. E. Peierls and R. H. Dalitz, *Selected scientific papers of Sir Rudolf Peierls: with commentary*, Vol. 19 (World Scientific, 1997).
- [47] K. Itô, *Encyclopedic dictionary of mathematics*, Vol. 1 (MIT press, 1993).
- [48] A. Kretinin, G. L. Yu, R. Jalil, Y. Cao, F. Withers, A. Mishchenko, M. I. Katsnelson, K. S. Novoselov, A. K. Geim, and F. Guinea, *Phys. Rev. B* **88**, 165427 (2013).
- [49] R. Kundu, *Modern Physics Letters B* **25**, 163 (2011).
- [50] P. Potasz, A. D. Güçlü, and P. Hawrylak, *Phys. Rev. B* **82**, 075425 (2010).
- [51] T. Ando, *Journal of the Physical Society of Japan* **75**, 074716 (2006).
- [52] A. D. Güçlü, P. Potasz, O. Voznyy, M. Korkusinski, and P. Hawrylak, *Phys. Rev. Lett.* **103**, 246805 (2009).
- [53] C. H. Lui, K. F. Mak, J. Shan, T. F. Heinz, *et al.*, *Phys. Rev. Lett.* **105**, 127404 (2010).
- [54] M. Breusing, S. Kuehn, T. Winzer, E. Malić, F. Milde, N. Severin, J. Rabe, C. Ropers, A. Knorr, and T. Elsaesser, *Phys. Rev. B* **83**, 153410 (2011).
- [55] E. Hwang, B. Y.-K. Hu, and S. D. Sarma, *Phys. Rev. B* **76**, 115434 (2007).
- [56] W.-K. Tse, E. Hwang, and S. Das Sarma, *Appl. Phys. Lett.* **93** (2008).
- [57] G. P. Zhang, M. S. Si, M. Murakami, Y. H. Bai, and T. F. George, *Nature Communications* **9**, 3031 (2018).
- [58] X.-M. Tong and S.-I. Chu, *Phys. Rev. A* **61**, 021802(R) (2000).
- [59] C. Trallero-Herrero, D. Cardoza, T. Weinacht, and J. Cohen, *Phys. Rev. A* **71**, 013423 (2005).
- [60] R. Jones, *Phys. Rev. Lett.* **74**, 1091 (1995).